Green synthesis of nanosized manganese dioxide as positive electrode for lithium-ion batteries using lemon juice and citrus peel

A. M Hashem, H. Abuzeid, M. Kaus, S. Indris, H. Ehrenberg, A. Mauger, C.M. Julien

Green synthesis of nanosized manganese dioxide as positive electrode for lithium-ion batteries using lemon juice and citrus peel

A.M. Hashem[1], H. Abuzeid[1], M. Kaus[2], S. Indris[2], H. Ehrenberg[2], A. Mauger[3], C.M. Julien[3]

[1]National Research Centre, Inorganic Chemistry Department, 33 El Bohouth St. (former El Tahrir St.), Dokki, Giza, Egypt, P.O.12622

[2]Karlsruhe Institute of Technology (KIT), Institute for Applied Materials (IAM), Hermann-von-Helmholtz-Platz 1, D-76344 Eggenstein-Leopoldshafen, Germany

[3]Sorbonne Université, UPMC Univ. Paris6, IMPMC, UMR 7590, 4 place Jussieu, 75252 Paris, France

Abstract

Nanosized MnO_2 powders were grown using a green synthesis based on citrates via redox reaction between $KMnO_4$ and natural reducing agents, i.e. lemon juice and peel extracts, without generating hazardous waste. X-ray diffraction (XRD) and Raman studies show that the samples grow as cryptomelane polymorph, α-MnO_2, crystallized with the tetragonal cryptomelane structure. Both J-MnO_2 prepared from lemon juice and P-MnO_2 prepared from citrus peel consist of nanosized particles as observed by scanning electron microscopy (SEM) and transmission electron microscopy (TEM). Thermogravimetric analysis (TGA) confirms the typical thermal decomposition of MnO_2 at temperatures of up to 500 ° C. Improved electrochemical properties are obtained and discussed for P-MnO_2, with a reversible capacity that reaches 160 mAh g^{-1} (initial capacity of 212 mAh g^{-1}) at a current density of 10 mA g^{-1} and a good rate capability.

Keywords: α-MnO_2; green synthesis; lemon peel; lemon juice; lithium batteries

Graphical Abstract

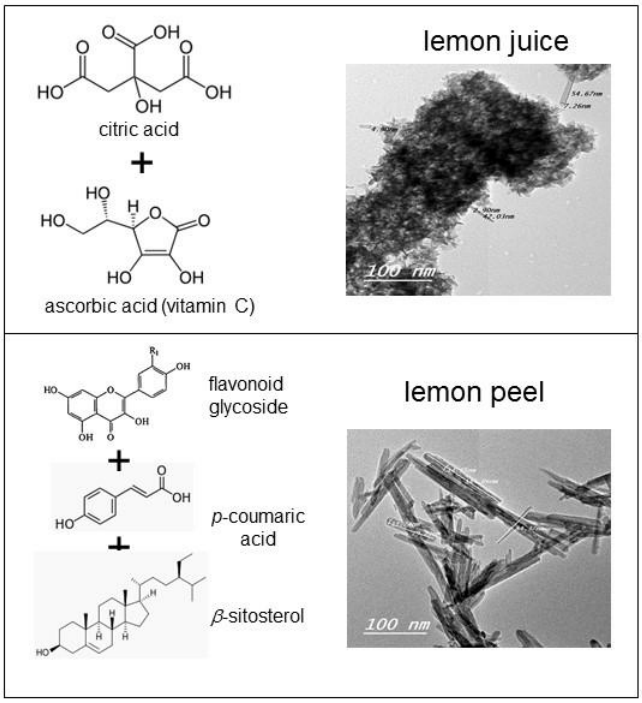

1. Introduction

Manganese dioxides (MDOs) have attracted great interest because of the variety of their structures and unique properties [1]. They find potential applications such as catalysts, solar cells and electrochemical capacitors, electrode materials of Li-ion and Li-air batteries [2-6] due to their low cost, earth abundance, environmental friendliness and variable oxidation states [7]. The structure of MDOs is built by an assembly of [MnO_6] octahedral units linked in different ways and forming cavities (tunnels) and thus different polymorphs. For instance, α-MnO_2 (cryptomelane) is constructed by edge and corner sharing of [MnO_6] along its *c* axis and displays the 2×2 tunnels architecture [8].

Submicronic materials, such as nanoparticles, nanorods, nanobelts, nanowires, nanotubes, nanofibers and urchins/orchids, mesoporous MDOs are currently investigated [9-11]. $KMnO_4$ is one of the main starting materials for synthesis of α-MnO_2 as it is not only a suitable Mn source, but it can also stabilize the crystallographic structure of MnO_2 by the presence of K^+ cations located in the cavities [12]. Based on redox reactions between MnO_4^- and Mn^{+2} species, MnO_2 nanomaterials have been successfully prepared by several methods, such as sol–gel, solid state reaction, electrochemical deposition, refluxing, hydrothermal and solvothermal routes [13-19]. The effect of synthetic parameters (e.g. pH value, synthesis temperature, and concentration of reactants) on the morphology of α-MnO_2 has been reported [8]. Subramanian [20] used a hydrothermal reaction at 140 °C for various reaction times (1–18 h) to synthesize MnO_2 nanorods using $MnSO_4 \cdot H_2O$ and $KMnO_4$ as starting materials. Xu et al. [21] prepared hollow spheres with a highly loose and mesoporous cluster structure of α-MnO_2 using $KMnO_4$, sulfuric acid and Cu scrap. Nanowhiskers and nanorods of MnO_2 were synthesized at 120 °C by a hydrothermal method using $KMnO_4$ and HNO_3 [22]. Liu et al. [23] succeeded to synthesize amorphous and spherical MDOs using $KMnO_4$, ethanol and sulfuric acid at pH=2 with particle sizes of about 100 nm at 60 °C. Also, the same reagents were used to synthesize α-MnO_2 nanowires with controllable size via a low-temperature hydrothermal route with a subsequent heat treatment, which showed promising electrochemical properties [24]. Feng et al. [25] used the one-pot hydrothermal synthesis to grow α-MnO_2 nanorods with an average diameter of 300 nm and length up to 1.2 mm, while Ji et al. [26] used a similar method to obtain longer α-MnO_2 nanorods.

In attempts to replace traditional chemical reducing agents such as ethanol, hydrazine hydrate, sodium borohydrate, formaldehyde, ethylene glycol, etc. by biological reagents containing anti-oxidative moieties such as flavonoids, tannins, vitamin C, etc., one can solve problems of cost and pollution [27]. Thus, many natural substances such as extracts of plants [28] can be used in "green synthesis" methods. Lemon juice is mostly water. The most important ingredient is citric acid, i.e. 5 vol.%, 48 g L^{-1}, next is malic acid, ascorbic acid (vitamin C: 40 mg per 100 g of lemon), and traces of tartaric acid [29].

For instance, extracts of peel of citrus fruits are directly reducing agents (antioxidant) [30] because they are rich sources of flavonoid glycoside, coumaric acid, β- and γ-sitosterol and volatile oils [31-34]. Extracts of lemon as rich sources of citric and ascorbic acid (vitamin C) were used to synthesize ZnO nanoparticles [35]. Ahmad et al. [36] pointed out that fibers of citrus fruit contain bioactive elements such as polyphenols and ascorbic acid, which promote the crystallization process of metal oxides.

In a recent review on nanostructured MnO_2 as electrode material for energy storage, we pointed out that the problems of the Zn/MnO_2 battery (limited cycling life and power) have now been entirely solved. The alkaline Zn/MnO_2 batteries now outperform the Li-ion batteries not only by the lower price, but also by their performance, both in energy and in power density [37]. In particular, Liu et al. reported such a battery, the capacity of which was 285 $mAh \cdot g^{-1}$ (MnO_2), with capacity retention of 92% over 5000 cycles [38]. MnO_2 is thus a promising candidate to be the electrode of next generation of commercial rechargeable batteries. The next problem is thus to optimize the synthesis of this material in terms of cost and environmental friendliness.

The present work addresses this problem by employing a facile, eco-friendly and cost-effective method using lemon juice and citrus peel to prepare α-MnO_2 nanomaterials, in which the reduction of $KMnO_4$ is ensured by the use of mixed bio-chelators including carboxylic groups. The as-prepared samples were characterized by XRD, TGA, SEM, TEM and Raman analyses. The electrochemical properties of both α-MnO_2 samples were evaluated by cyclic voltammetry and galvanostatic charge-discharge processes.

2. Experimental

Two MnO_2 samples were prepared by green synthesis using fresh lemon juice (final product named J-MnO_2) and extract of lemon peel (final product named P-MnO_2). Pieces of fresh lemon were washed and squeezed to prepare 40 ml of juice, which was boiled for 10 minutes, filtered and completed with distilled water after boiling to have 50 ml then stirred again for 15 minutes at room temperature followed by a final filtration. This extract of juice was added to 4.7 g $KMnO_4$, dissolved in 100 ml of water and acidified with 2 ml of 2.5 mol L^{-1} H_2SO_4. After stirring vigorously for 1 h at room temperature, this mixture changed in color from purple to black due to the complete reduction of $KMnO_4$ by the juice. The precipitate was isolated by filtration and washed several times with distilled water to remove potassium ions. The collected precipitate was dried overnight at 90 °C and then calcined at 300-400 °C for 5 hours in ambient atmosphere.

P-MnO_2 was prepared through redox reaction between $KMnO_4$ and lemon peel. 10 g of peel of lemon were successively washed, dried at 90 °C, and boiled in distilled water for 10 min at 100 ^oC. The peel extract was filtered and completed to 50 ml with distilled water by stirring for 15 minutes at room temperature followed by another filtration. The extract was added to 2.5 g $KMnO_4$, dissolved in 100 ml of water and finally treated by the same manner described above.

The crystal structure was determined by XRD analysis using a STOE STADI P diffractometer with curved Ge 111 monochromator and Mo $K_{\alpha 1}$ radiation and a Mythen 1K strip detector (50 μm strip pitch DECTRIS). Rietveld refinements were performed by the FULLPROF program [39,40]. TGA measurements were carried out using a thermal gravimetric analyzer (Perkin Elmer, TGA 7 series) in the temperature range of 50–1000 °C in air at a heating rate of 10 ^oC min^{-1}. The morphology and structure of the samples were further investigated by field emission scanning electron microscopy (FESEM, Quanta FEG 250), and high-resolution transmission electron microscopy (HRTEM, JEOL, JEM-2100, Electron microscope, Japan). Raman spectra were collected on a LabRam Evolution HR (HORIBA) spectrometer equipped with a Nd:YAG laser (523 nm, 1 mW). The final spectra consist of two independent acquisitions with a total acquisition time of 720 s.

Electrochemical properties of MnO_2 electrodes were carried out in Swagelok-type cells. The active material was mixed with carbon black (Super P, Timcal) and PVDF in the ratio 80:15:5. The cathode loading was ~4 mg cm^{-2}. Two layers of Whatman GF/B separators and 1 mol L^{-1} $LiPF_6$ in a 1:1 mixture of ethylene carbonate and dimethyl carbonate were used for the cell assembly. Lithium metal was used as the counter electrode. The material was characterized galvanostatically using the cycling station model Lithium Cell Cycler, KIT. Cyclic voltammograms (CV) were recorded using a VMP3 potentiostat (Biologic Science Instruments, France) at a sweep rate of 0.1 mV s^{-1}.

3. Results and discussion

3.1. Structural properties

Figures 1a-b display the X-ray diffraction patterns of the green synthesized samples using lemon peel extract (P-MnO_2) and lemon juice (J-MnO_2), respectively. All the XRD peaks can be readily indexed to α-MnO_2 (JCPDS, 44-0141). A Rietveld refinement of the underlying structure model, based on the cryptomelane polymorph noted α-MnO_2, was applied for P-MnO_2. The comparison between observed and calculated patterns is shown in Fig. 1a together with their difference curve. The structure parameters of the tetragonal structure (space group *I*4/*m*) are summarized in Table 1. Residual potassium in the structure is detected, corresponding to the composition $K_{0.12}MnO_2$. The potassium distribution is smeared out along the (0,0,z) tunnels, best described by two partially occupied sites K1 and K2. The 002 reflection has a much smaller half-width, which is only determined from the projection of the electron density on the c-axis and not affected by any disorder in the *ab*-plane. In contrast, despite the optimization of the sintering temperature at 340 °C, J-MnO_2 does not show sufficient long-range order for a reasonable Rietveld refinement. A comparison between the observed diffraction patterns for J-MnO_2 and for an empty capillary is shown in Fig. 1b. The maximum intensity corresponds to the position of the strongest reflection (121) of the cryptomelane structure.

It is well known that large K^+ cations are inserted into the tunnel cavity (2*e* Wyckoff site) during synthesis of the α-MnO_2 hollandite structure [41,42]. The presence of K^+ is the key parameter, which governs the properties of these materials. Recently,

Yuan et al. investigated the influence of potassium cations on the electrochemical properties of α-MnO_2. The role of cations inside 2×2 tunnels has three beneficial effects: (i) increase of the electronic conductivity of the host, (ii) improve the Li^+ diffusivity and (iii) introduce a structural transition during lithiation for high K^+ concentration, i.e. x=0.25 [41,43]. This large cation is essential for the formation and stabilization of α-MnO_2 lattice [44] and leads to the mixed valence state of Mn^{4+} and Mn^{3+} ions that depends of the potassium concentration. K^+ ions increase the concentration of less-localized e_g d-electrons of the Mn^{3+} ions. Especially, Luo et al. [45] demonstrated that the α-$K_{0.12}MnO_2$ specimen is homogeneous with the Mn ions in the average oxidation state.

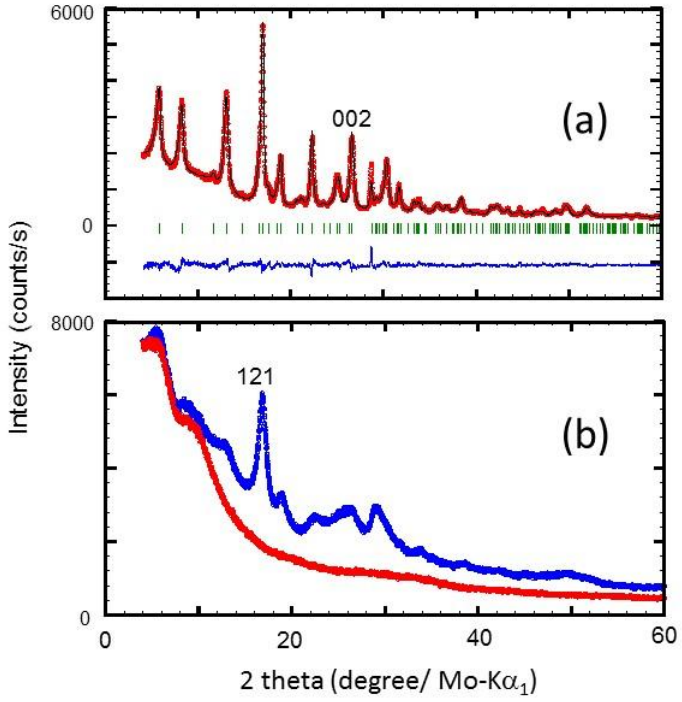

Fig. 1. X-ray powder diffraction patterns of green synthesized MnO_2 using (a, left) lemon peel extract, P-MnO_2 and (b, right) lemon juice, J-MnO_2. The results of a Rietveld refinement is shown for P-MnO_2 with refined composition $K_{0.12}MnO_2$ in (a). A comparison between XRD patterns from J-MnO_2 and the empty capillary is shown in (b), because of a lack of sufficient long-range order. Two characteristic reflections are labelled.

The short-range structural properties of the prepared samples were further investigated by Raman spectroscopy. Figure 2 displays the Raman spectra of J-MnO_2 and P-MnO_2 in the spectral domain 100-1000 cm^{-1} of the fundamental vibrations of the MnO_2 tetragonal lattice. For P-MnO_2, well-resolved Raman bands located at 180, 205, 300, 330, 390, 475, 515, 577, 638 and 750 cm^{-1} are characteristic of α-MnO_2 phase, while the spectrum of J-MnO_2 displays broaden bands because the nearly amorphous state of this sample. However, the high-frequency bands clearly identified at 515, 577 and 638 cm^{-1} and the weak bands at 390 and 180 cm^{-1} match well with the tetragonal unit cell (space group *I*4/m; spectroscopic symmetry C^5_{4h}). Shortly, the Raman band at 180 cm^{-1} is due to the translational motion of the MnO_6 octahedra (lattice mode), the band at 390 cm^{-1} is attributed to the Mn–O bending vibrations, while the high-frequency bands at 577 and 638 cm^{-1} originate from the stretching vibrations of MnO_6 octahedra within the tetragonal lattice [46,47]. These results appear to be in good agreement with those obtained by X-ray diffraction as the degree of crystallinity also affects the local atomic environment, i.e. the strength of the Raman modes.

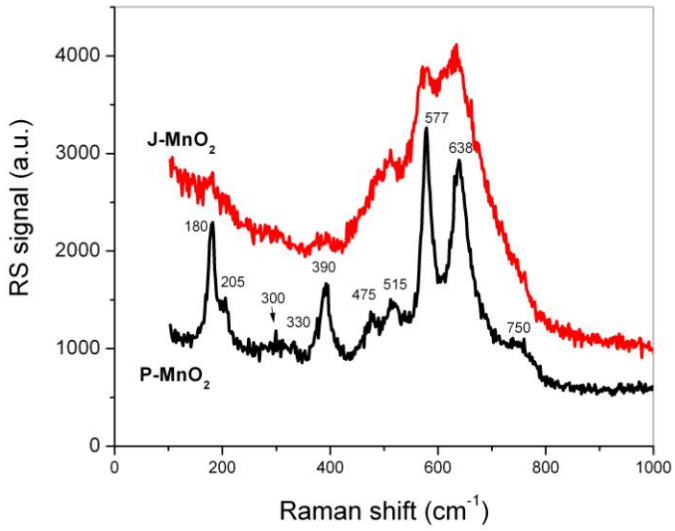

Fig. 2. Raman scattering spectra of α-MnO_2 nanostructured powders prepared by lemon juice (J-MnO_2) and lemon peel (P-MnO_2).

The difference between the XRD patterns of J-MnO_2 and P-MnO_2 and between the Raman spectra as well are attributed to the different degrees of crystallinity for both

samples, which originates from the nature of reducing reagents that have been used. It is well-known that the chelate-assisted sol-gel method with different carboxylic acids can result in markedly different structural defects and morphologies of products [48]. However, in the sol–gel method, the choice of chelators often directly affects electrochemical properties of the products. For example, when only citric acid is used as chelating agent, some issues will appear in the process of heat treatment due to the existence of segregation phenomenon in the precursors [49]. By employing a mixture of chelators, these disadvantages can be overcome, which provides a homogeneous distribution of uniform nanosized particles with good stoichiometry control of the final product. Such a procedure has been recently applied to prepare Li-rich cathode materials [50]. In this work, we compare two mixed chelators with different molecular architectures (Fig. 3), which belong to the class of bio-reagents present in citrus fruits [35]. As a result, the reduction of potassium permanganate appeared very sensitive to the complexing reagent, i.e. the bonding of -COOH- carboxylic groups, which makes a big difference in the crystallization of MnO_2. Powders grown by the lemon juice-assisted route exhibit a highly disordered structure even at the local scale observed by Raman spectroscopy, whereas P-MnO_2 samples synthesized with extracts of lemon peel present a better crystallinity of the nanostructured particles owing to the complex molecular moieties involved in the reduction process acting as fuels for the MnO_2 crystallization.

The ill-resolved bands of the Raman spectrum of the J-sample shows that even the molecular scale is affected, despite the large size of the crystallites (2.4 nm). This is attributed to the fact that the strain field generated by the grain boundaries is long range in nature, i.e. a range that is of the same order of magnitude as the crystallite size. This strain field thus creates lattice distortions that extend to the same size, which explains not only the lack of resolution of the Raman spectrum, but also explains the lack of long-rage crystalline order as observed by X-ray diffraction. Another reason for the poorly resolved Raman spectrum could be that a rather random distribution of K^+ in the tunnels is blocking and coupling some vibrational modes.

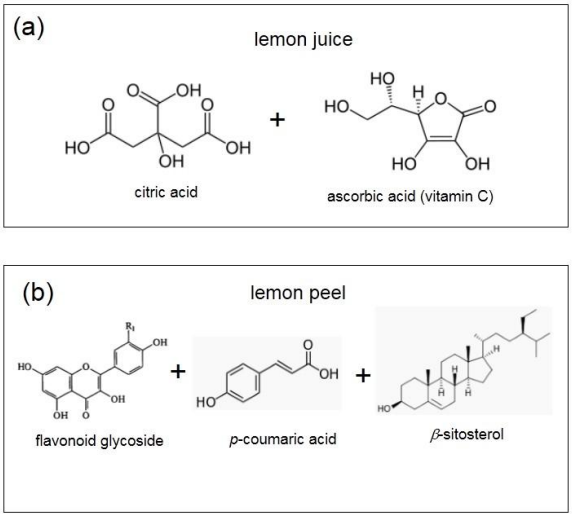

Fig. 3. Molecular representation of anti-oxidative moieties present in citrus fruits. (a) lemon juice and (b) lemon peel.

3.2. Thermal stability

Figures 4a-b show the thermogravimetric analyses (TGA) of the J-MnO_2 and P-MnO_2 as-prepared samples, respectively. These TGA curves have almost the same thermal behavior typical of MDOs. The gradual weight loss observed in the range 25-250 ^{o}C with a weight loss of ca. 10 % is assigned to the release of predominantly adsorbed water and weakly bounded water molecules present in the sample and trace amounts of oxygen [51]. The second gradual weight loss is attributed to the formation of highly crystallized α-MnO_2 followed by an endothermic reaction which is due to the removal of oxygen and the conversion of α-MnO_2 to α-Mn_2O_3 phase. This distinct transformation is observed at 530 and 600 °C for J-MnO_2 and P-MnO_2, respectively. The third weight loss recorded at T>900 °C is attributed to further oxygen loss and the formation of the Mn_3O_4 spinel structure [47]. The shape of thermograms as well as phase transitions shown in Fig. 4 are in good agreement with the literature [52-54].

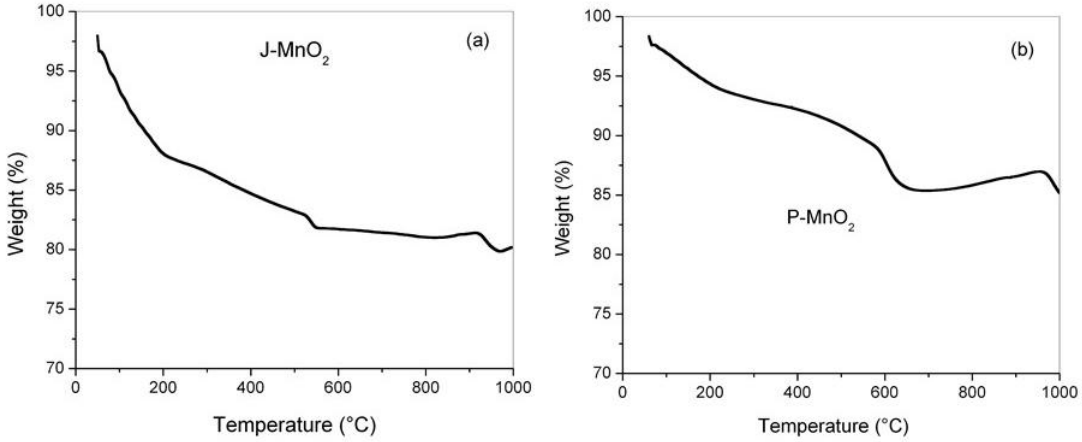

Fig. 4. Gravimetric thermograms of green synthesized samples (a) J-MnO_2 and (b) P-MnO_2 in air.

3.3. Morphology

Figure 5 (a-d) show the SEM and TEM images of green-synthesized MnO_2 samples. Two different morphologies are clearly evidenced. As shown in Fig. 5a, the sample prepared via lemon juice consists of agglomerates of very fine particles of less than 10 nm size (Fig. 5c). Few particles have the tendency to grow with a nanoneedle-like shape (~50 nm length). In contrast, the sample prepared via lemon peel has a different morphology. The poor crystallization of the J-MnO_2 sample explains the irregular form of the particles, but also is an obstacle to the growth of the particles during the synthesis after their nucleation, which explains the smaller size of the primary particles. As shown in Fig. 5d, P-MnO_2 consists of fairly uniform nanorods with an average size about 17 nm in diameter and 150 nm in length. From the above described investigations, it is clearly demonstrated that the nature of the reducing reagent has a strong effect on the morphology of α-MnO_2 particles. It is the combination of citric and ascorbic acids that provide the smallest nanosized particles, while the complex reducing reagent of lemon peel favors the growth of regular nanorod-like materials. Note that among anti-oxidative moieties in Fig. 3b, *p*-coumarin acid is the most abundant phenolic compound in citrus peel, while β-sitosterol belongs to the class of "plant sterol" with a chemical structure similar to that of cholesterol, and flavonoid glycosides are primarily anti-oxidative components in the lemon peel. Currently, α-MnO_2 nanorods are synthesized by adopting

a hydrothermal process based on $KMnO_4$ and $MnSO_4$ as the reactants [55-56]. In this work, we have obtained the same sample morphology of α-MnO_2 crystalline nanorods using a facile and low-cost synthetic process.

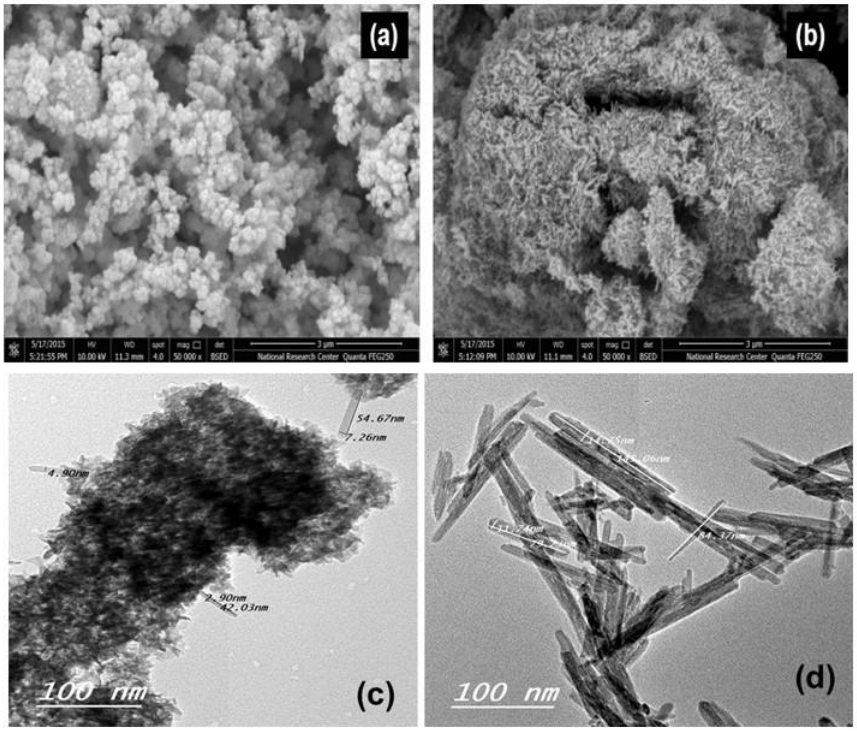

Fig. 5. (a,b) SEM images of green synthesized samples (a) J-MnO_2 and (b) P-MnO_2 and (c,d) TEM images of green synthesized samples (c) J-MnO_2 and (d) P-MnO_2.

3.4. Electrochemical tests

MnO_2 powders were electrochemically tested by cyclic voltammetry and galvanostatic charge-discharge cycles in the voltage range 1.5 – 3.5 V vs. Li^+/Li^0 at different current densities from 10 to 400 mA g^{-1} (1C=260 mA g^{-1}). The cyclic voltammograms (CVs) of the first 20 cycles are displayed in Fig. 6. It is well known that lithium ions are accommodated on off-center 8*h* Wyckoff positions inside α-MnO_2 2×2 tunnels that determine the overall discharge capacity [41].

During the first discharge process both CVs are dominated by a broad current peak around 2.5 V. The broadness of redox peaks is attributed to the poor crystallinity and/or the morphology of α-MnO_2 nanopowders. The shift of the reduction peak from 2.5 V at

the first discharge cycle to 2.65 V for the forthcoming cycles is assigned to the lithium-cell formation and to the small amount of remaining Li ions inserted in the initial discharge reaction, i.e. the so-called loss of lithium inventory (LLI). This type of structural evolution is currently observed for the hollandite α-MnO_2 electrode [36,58]. Ching et al. [59] have reported the change in peak position as a structural change associated with γ-MnO_2, which does not occur in our case. CV curves show clearly that the host structure is stabilized by partial lithiation of α-Li_xMnO_2. This stabilization is obviously observed for the subsequent cycles (Fig. 6), for which the set of intense redox peaks is located around 3.15 and 2.65 V, and the differential peak potential between E_{ox} and E_{red} is 0.5 V. This value is higher than the one reported for micro-sized materials [60] and did not vary significantly in the subsequent cycles. Tompsett et al. [61] suggested that lithium ions are preferentially located at the off-center 8*h* sites, near the walls of the 2×2 tunnels for the initial stage of lithiation ($0 \leq x \leq 0.5$ in α-Li_xMnO_2), while 8*h*' sites are occupied for a high concentration Li^+ ions in α-$Li_{0.75}MnO_2$ because of the different energies of formation. Both samples have a similar behavior for the subsequent discharge cycles. The most distinct features for green synthesized MnO_2 electrodes are the set of small redox peaks located at 2.6 and 2.3 V, which gradually decrease as the cell is cycled. In case of the P-MnO_2 sample, the reduction process is characterized by an additional reduction peak located at 2.8 V. These features are attributed to the effect of the insertion-deinsertion mechanism in MnO_2 nanocrystallites with sizes smaller than 10 nm.

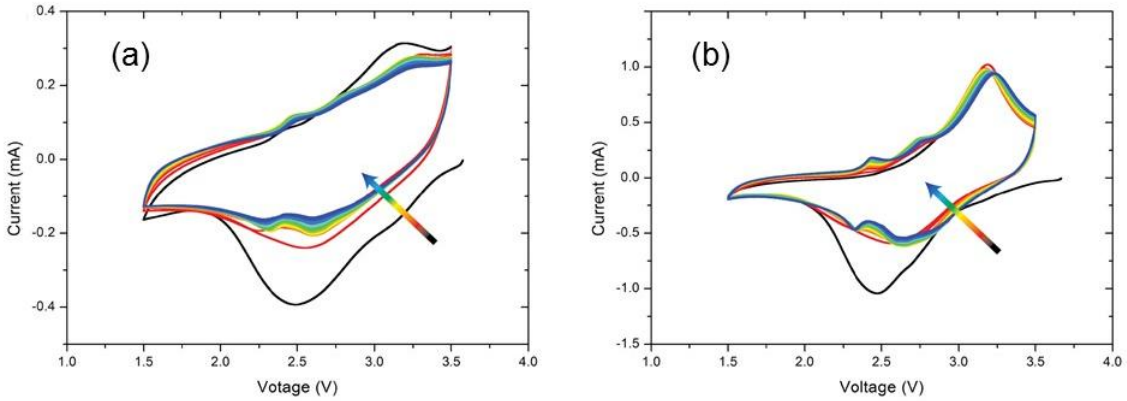

Fig. 6. Cyclic voltammograms of the first 20 cycles (from black via red, yellow and green to blue) samples (a) J-MnO_2 and (b) P-MnO_2 carried out at sweep rate of 0.1 mV s^{-1}.

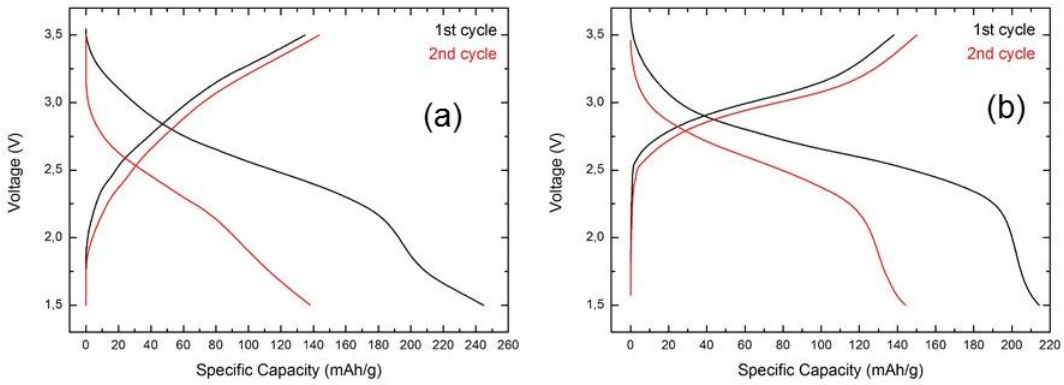

Fig. 7. Charge-discharge voltage profiles of MnO_2//Li cells with (a) J-MnO_2 and (b) P-MnO_2 cathode materials. Measurements were carried out at current of 10 mA g^{-1}. S1 and S2 are the slope $\Delta V/\Delta Q$ of the potential profile at $Q_{max}/2$.

The galvanostatic discharge-charge profiles of the Li//α-MnO_2 cells are presented in Fig. 7. Measurements were carried out in the voltage range 1.5 – 3.5 V vs. Li^+/Li^0 at a current density of 10 mA g^{-1} (C/26). These results show several features: (i) the first cycle is dominated by a distinct irreversible capacity for both materials, (ii) the degree of crystallinity affects the shape of discharge-charge profiles, (iii) the charge pseudo plateau is clearly observed in highly crystallized P-MnO_2 sample, while the discharge-charge curves of J-MnO_2 display a rather S-shape characteristic of a disordered material, (iv) a noticed difference is observed in the voltage curve at the end of the discharge process. The initial discharge specific capacity of J-MnO_2 is ~245 mAh g^{-1}, whereas subsequent discharging reactions achieve only a specific capacity of ~135 mAh g^{-1}. The same situation is observed in the case of P-MnO_2 with an initial specific capacity of ~214 mAh g^{-1}. This can be attributed to the size of nanoparticles that results in a high specific surface area (BET≈12 m^2 g^{-1}) and thus an increase of the effective interface between material and electrolyte. The best electrochemical behavior of the P-MnO_2 electrode is evidenced by the estimation of the slope $\Delta Q/\Delta V$ of the discharge curves. One finds $\Delta Q/\Delta V$= 180 mAh g^{-1} V^{-1} for J-MnO_2 and $\Delta Q/\Delta V$=294 mAh g^{-1} V^{-1} for P-MnO_2. On the other hand, the situation is reversed as soon as the second cycle is carried out (see Fig. 7). In both samples, the irreversible capacity decreases and the coulombic efficiency increases after the first cycle. These results match well with electrochemical data reported

in Ref. [43] for samples prepared by wet-chemical methods. From the second cycle to the 5th cycle, the discharge capacity of the J-MnO_2 sample increases from 135 mAh g^{-1} to 145 mAh g^{-1}, due to the formation of the solid-electrolyte interface, and the fact that additional sites at the surface are available at the surface of the particles. The better performance is even more pronounced when considering the rate capacity reported in Fig. 8 for discharge current densities in the range 10-400 mA g^{-1}. A reversible specific capacity of 50 mAh g^{-1} is delivered for the P-MnO_2 cell at 400 mA g^{-1}, while that of the J-MnO_2 has vanished, an evidence for the sluggish kinetics associated to the lattice disorder. The coulombic efficiency for the first charge of both samples is small, but on the second cycle the cells show good rechargeability with efficiency close to 99%. Fig. 8b presents the cycleability for J-MnO_2 and P-MnO_2 electrodes. After 50 cycles, the capacity retention of P-MnO_2 got restored to 73%, while it was 55% for J-MnO_2. The better electrochemical performance of P-MnO_2 is attributed to its crystallinity as reported in the structural section.

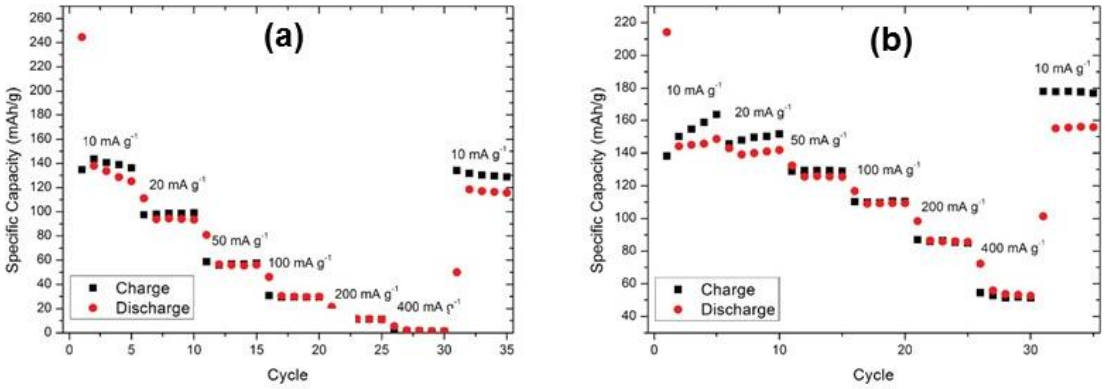

Fig. 8. Rate capability tests of Li half cells for (a) J-MnO_2 and (b) P-MnO_2.

4. Conclusion

The green synthesis of MnO_2 prepared with either the juice (J) or the peel (P) of lemon has been successfully achieved. Both the crystallization and the electrochemical properties are improved in the P-MnO_2 with respect to J-MnO_2. This is attributed to the fact that the lemon peel contains three reducing (anti-oxidative) reagents (and volatile oils), while the juice of lemon contains only citric and ascorbic (Vitamin C) acids, which leads to better results than those obtained with only one of these two acids, but still less

than the three active elements in the peel. The electrochemical properties of the P-MnO_2 are as good as those obtained with the traditional chemical reducing reagents that are both costly and polluting. This new synthesis is straightforward and inexpensive then allows for a synthesis process that is green, cheaper, and easily scalable for mass production of α-MnO_2 that has many applications in the industry, including electrochemical energy storage.

Acknowledgement

Some part of this work has benefited from financial support within the BMBF project "DESIREE", grant number 03SF0477B.

References

1. Wei W, Cui X, Chen W, Ivey DG (2011) Manganese oxide-based materials as electrochemical supercapacitor electrodes. Chem Soc Rev 40:1697-1721
2. A. Debart, A.J. Paterson, J. Bao, P.G. Bruce, Angew Chem. Int. Ed. 47 (2008) 4521.
3. S.L. Chou, J.Z. Wang, S.Y. Chew, H.K. Liu, S.X. Dou, Electrochem. Commun. 10 (2008) 1724.
4. J. Lee, J.M. Lee, S. Yoon, S.O. Kim, J.S. Sohn, K.I. Rhee, J. Power Sources 183 (2008) 325.
5. T.X.T. Sayle, R.R. Maphanga, P.E. Ngoepe, D.C. Sayle, J. Am. Chem. Soc. 131 (2009) 6161.
6. S. Ida, A.K. Thapa, Y. Hidaka, Y. Okamoto, M. Matsuka, H. Hagiwara, T. Ishihara, J. Power Sources 203 (2012) 159.
7. Y. Wang, P. Ding, C. Wang, Fabrication and lithium storage properties of MnO_2 hierarchical hollow cubes, J. Alloys Compd 654 (2016) 273.
8. R. Han, Sh. Xing, Z. Ma, Y. Wu, Y. G. Han, Sh. Xing, Z. Ma, Y. Wu, Y. Gao, J. Mater Sci 47 (2012) 3822.
9. H. Zhang, G. P. Cao, Y. S. Yang, Z. N. Gu, J. Electrochem. Soc. 155 (2008) K19.
10. M. S. Wu, P. J. Chiang, J.T. Lee, J. C. Lin, J. Phys. Chem. B 109 (2005) 23279.

11. E. S. Toberer, T. D. Schladt, R. Seshadri, J. Am. Chem. Soc. 128 (2006) 1462.
12. X. Huang, D. Lv, H. Yue, A. Attia, Y. Yang, Nanotechnology 19 (2008) 225606.
13. X. Hong, G. Zhang, Y. Y. Zhu, H. Yang, Mater. Res Bull 38 (2003) 1695-1703.
14. S. X. Yang, H. Y. Yang, H. Y. Ma, S. Guo, F. Cao, J. Gong, Y. L. Deng, Chem. Commun. 47 (2011) 2619.
15. Z.P. Feng, G. Li, J.H. Zhong, Z.L. Wang, Y.N. Ou, Y.X. Tong, Electrochem. Commun. 11 (2009) 706.
16. N. Wang, X. Cao, L. He, W. Zhang, L. Guo, C. P. Chen, R. M. Wang, S. H. Yang, J. Phys. Chem. C 112 (2008) 365.
17. Y. Chen, YZ. Hong, YP. Ma, JB. Li, J Alloys Compd 490 (2010) 331.
18. G.H. Yue, P.X. Yan, Yan D, D. M. Qu, X. Y. Fan, M. X. Wang, H. T. Shang, J Cryst Growth 294 (2006) 385.
19. D.S. Zheng, Z.L. Yin, W.M. Zhang, X.J. Tan, S.X. Sun, Cryst Growth Des 6 (2006) 1733.
20. V. Subramanian, H. W. Zhu, R. Vajtai, P. M. Ajayan, B. Q. Wei, J. Phys. Chem. B 109 (2005) 20207.
21. C. Xu, B. Li, H. Du, F. Kang, Y. Zeng, J. Power Sources 180 (2008) 664.
22. N Tang, X. Tian, C. Yang, Z. Pi, Mater. Res. Bull. 44 (2009) 2062.
23. J.-L Liu, L.-Z Fan, X. Qu, Electrochim. Acta 66 (2012) 302.
24. Z. Hu, S. Zhu, H. Huang, J. Zhang, Y.Xu, J. Crystal Growth 434 (2016) 7.
25. J. Feng, P. Zhang, A. Wang, Y. Zhang, W. Dong, J. Chen, J. Colloid Int. Sci. 359 (2011) 1.
26. Z.H. Ji, B. Dong, H.L. Guo, Y.M. Chai, Y.-P. Li, Y.-Q. Liu, C.-G. Liu, Mater. Chem. Phys. 136 (2012) 831.
27. R. Praphulla, M. S. Chandraprasad, Y.N. Lakshmi, R. Jahnavi, P. Aishwarya, Sh. Srinidhi, Inter. J. Multidiscipl. Current Res. 2 (2014) 165.
28. E. Rodríguez-León, R. Iñiguez-Palomares, R. E. Navarro, R. Herrera-Urbina, J. Tánori, C. Iñiguez-Palomares, A. Maldonado, Nanoscale Res. Lett. 8 (2013) 1.
29. http://www.lemon-info.com/2009/04/18/what-is-lemon-juice-made-of/
30. J. Maruti.-Dhanavade, C. B. Jalkute, S. Jai. G. Kailash D. Sonawane, British J. Pharmacol. Toxicol. 2 (2011) 119.

31. S.M. Shahnah, S. Ali, H. Ansari, P. Bagri, Burn. F. Sci. Pharm., 75 (2007) 165.
32. R. Munakata, T. Inoue, T. Koeduka, K. Sasaki, Y. Tsurumaru, A. Suguyama, Y. Uto, H. Hori, J. Azuma, K. Yazaki, Biosci. Biotechnol. Biochem. 76 (2012) 1389.
33. L. Kamaliroosta, M. Zolfaghari, S. Shafiee, K. Larijani, M. Zojaji, J. Food Biosci. Technol. 6 (2016) 69.
34. E.D. Lund, W.L. Bryan, J. Food Sci. 41 (1976) 1194.
35. N. A. Samat, R.M. Nor, Ceramics Inter. 39 (2013) S545.
36. M.M. Ahmad, Z. Salim-ur-Rehman, F.M. Iqbal-Anjum, J.I. Sultan, Pak. J. Bot., 38 (2006) 319.
37. C. M. Julien, A. Mauger, Nanomaterials 7 (2017) 396.
38. T. Liu, C. Jiang, W. You, J. Yu, J. Mater. Chem. A 5 (2017) 8635.
39. J. Rodriguez-Carjaval, Physica B 192 (1993) 55.
40. H.P Klug, L.E. Alexander, X-ray Diffraction Procedures for polycrystalline and Amorphous Materials, Wiley, New York, 1974.
41. Y. Yuan, A. Nie, G.M. Odegard, R. Xu, D. Zhou, S. Santhanagopalan, K. He, H. Asayesh-Ardakani, D.D. Meng, R.F. Klie, C. Johnson, J. Lu, R. Shahbazian-Yassar, Nano Lett. 15 (2015) 2998.
42. D. Zai, B. Li, C. Xu, H. Du, Y. He, C. Wei, F. Kang, J. Power Sources 196 (2011) 7860.
43. Y. Yuan, C. Zhan, K. He, H. Chen, W. Yao, S. Sharifi-Asl, B. Song, Z. Yang, A. Nie, X. Luo, H. Wang, S.M. Wood, K. Amine, M.S. Islam, J. Lu, R. Shahbazian-Yassar, Nat. Commun. 7 (2016) 13374.
44. X. Wang, Y. Li, J. Am. Chem. Soc. 124 (2002) 2880.
45. J. Luo, H.T. Zhu, J.K. Liang, G.H. Rao, J.B. Li, Z.M. Du, J. Phys. Chem. C 114 (2010) 8782.
46. J. Vicat, E. Fanchon, P. Strobel, Duc Tran Qui, Acta Cryst. B42 (1986) 162.
47. A.M Hashem, A.M. Abdel-Latif, H.M. Abuzeid, H.M. Abbas, H. Ehrenberg, R.S. Farag, A. Mauger, C.M. Julien, J. Alloys Compd 509 (2011) 9669.
48. G. Tao, F. Helmer, N. Poul, Anal. Chim. Acta 648 (2009) 235-239.
49. S. Bach, J.P. Pereira-Ramos, N. Baffier, J. Power Sources 81–82 (1999) 273.
50. Z. Wang, F. Wu, Y.F. Su, Acta Phys. Chim. Sin. 28 (2012) 823.

51. C. Tsang, J. Kim, A. Manthiram, J. Solid State Chem. 137 (1998) 28.
52. Y.U. Jeong, A. Manthiram, J. Electrochem. Soc. 149 (2002) A1419.
53. J.K. Chang, Y.-L. Chen, W.-T. Tsai, J. Power Sources 135 (2004) 344.
54. S. Devaraj, N. Munichandraiah, J. Electrochem. Soc. 154 (2007) A80.
55. D. Liao, C. Xia, X. Xi, C. Zhou, K. Xiao, X. Chen, S. Qin, J. Sol-Gel Sci. Technol. 78 (2016) 403.
56. A.M. Hashem, H.M. Abuzeid, D. Mikhailova, H. Ehrenberg, A. Mauger, C.M. Julien, J. Mater. Sci. 47 (2012) 2479.
57. F. Cheng, Y. Su, J. Liang, Z. Tao, J. Chen, Chem. Mater. 22 (2010) 898.
58. C.S. Johnson, D.W. Dees, M.F. Mansuetto, M.M. Thackeray, D.R. Vissers, D. Argyriou, C.K. Loong, L.J. Christensen, J. Power Sources 68 (1997) 570.
59. S. Ching, J.A. Landrigan, M.L. Jorgensen, N. Duan, S.L. Suib, C.L. O'Young, Chem. Mater. 7 (1995) 1604
60. C.S. Johnson, D.W. Dees, M.F. Mansuetto, M.M. Thackeray, D.R. Vissers, D. Argyriou, C.K. Loong, L. Christensen, J. Power Sources 68 (1997) 570-577
61. D.A.Tompsett, M.S. Islam, Chem. Mater. 25 (2013) 2515.

Figure captions

Fig. 1. X-ray powder diffraction patterns of green synthesized MnO_2 using (a, left) lemon peel extract, P-MnO_2 and (b, right) lemon juice, J-MnO_2. The results of a Rietveld refinement is shown for P-MnO_2 with refined composition $K_{0.12}MnO_2$ in (a). A comparison between XRD patterns from J-MnO_2 and the empty capillary is shown in (b), because of a lack of sufficient long-range order. Two characteristic reflections are labelled.

Fig. 2. Raman scattering spectra of α-MnO_2 nanostructured powders prepared by lemon juice (J-MnO_2) and lemon peel (P-MnO_2).

Fig. 3. Molecular representation of anti-oxidative moieties present in citrus fruits. (a) lemon juice and (b) lemon peel.

Fig. 4. Gravimetric thermograms of green synthesized samples (a) J-MnO_2 and (b) P-MnO_2 in air.

Fig. 5. (a,b) SEM images of green synthesized samples (a) J-MnO_2 and (b) P-MnO_2 and (c,d) TEM images of green synthesized samples (c) J-MnO_2 and (d) P-MnO_2.

Fig. 6. Cyclic voltammograms of the first 20 cycles (from black via red, yellow and green to blue) samples (a) J-MnO_2 and (b) P-MnO_2 carried out at sweep rate of 0.1 mV s^{-1}.

Fig. 7. Charge-discharge voltage profiles of MnO_2//Li cells with (a) J-MnO_2 and (b) P-MnO_2 cathode materials. Measurements were carried out at current of 10 mA g^{-1}. S1 and S2 are the slope $\Delta V/\Delta Q$ of the potential profile at $Q_{max}/2$.

Fig. 8. Rate capability tests of Li half cells for (a) J-MnO_2 and (b) P-MnO_2.